REVISION 1

Petalite under Pressure: Elastic Behavior and Phase Stability

Nancy L. Ross,[1*] Jing Zhao,[1] Carla Slebodnick,[2] Elinor C. Spencer, [1] and Bryan C. Chakoumakos[3]

[1,2] Depts. of Geosciences[1] and Chemistry[2], Virginia Tech, Blacksburg, VA 24061, USA

[3] Quantum Condensed Matter Division, Oak Ridge National Laboratory, P.O. Box 2008 MS-6393, Oak Ridge, TN 37831-6393, USA

Abstract

The lithium aluminosilicate mineral petalite ($LiAlSi_4O_{10}$) has been studied using high-pressure single-crystal X-ray diffraction (HP-XRD) up to 5 GPa. Petalite undergoes two fully reversible pressure-induced first-order phase transitions, not previously reported in the literature, at *ca*. 1.5 and 2.5 GPa. The first of these transforms the low-pressure α-phase of petalite (*P*2/*c*) to an intermediate β′-phase that then fully converts to the high-pressure β-phase at *ca*. 2.5 GPa. The $\alpha \rightarrow \beta$ transition is isomorphic and is associated with tripling of the unit cell volume. Analysis of the HP-XRD data show that although the fundamental features of the petalite structure are retained through this transition, there are subtle alterations in the internal structure of the silicate double-layers in the β-phase relative to the α-phase. Measurement of the unit cell parameters of petalite as a function of pressure, and fitting of the data with 3rd order Birch-Murnaghan equations of state, has provided revised elastic constants for petalite. The bulk moduli of the α and β-phases are 49(1) and 35(3) GPa, respectively. These values indicate that the compressibility of the-α phase of petalite lies between the alkali feldpsars and alkali feldspathoids, whereas the β-phase has a compressibility more comparable with layered silicates. Structure analysis

has shown that the compression of the α-phase is facilitated by the rigid body movement of the Si_2O_7 units from which the silicate double-layers are constructed.

Keywords: Petalite, high-Pressure, single-crystal X-ray diffraction, equation of state, phase transition

Introduction

The lithium aluminosilicate mineral petalite is one of the three most abundant naturally occurring lithium-rich minerals, and is of fundamental relevance in the evaluation of conditions associated with magmatic pegmatite crystallization processes. The crystal chemistry of the low-pressure α-phase of petalite has been the subject of extensive study (Černý & London, 1983 and references therein).

The petalite structure can be described as a 3-dimensional $AlSi_4O_{10}$ framework consisting of puckered double-sheets of corner sharing SiO_4 tetrahedra stacked parallel to the (100) plane with corner-sharing AlO_4 tetrahedra that bridge neighboring layers (Fig. 1). The neutrality of the structure is ensured by the presence of lithium cations residing within channels that propagate through the structure in the [101] direction. The Li cations are bonded to four oxygen atoms and the resulting LiO_4 polyhedra possess geometries that are intermediate between those of an idealized tetrahedron and a perfect square planar arrangement. Both spectroscopic and diffraction studies have shown that all cation sites within naturally occurring specimens of petalite are fully ordered (Černý & London, 1983; Tagai et al., 1982) and our data concur with this finding.

The structure of petalite was originally reported in the non-standard *P*2/*a* setting of space group *P*2/*c* (Tagai et al., 1982). However, for the high pressure X-ray diffraction

(HP XRD) analysis discussed in this contribution we have chosen to represent, for consistency and ease of scrutiny, all petalite phases in a standard *P*2/*c* setting. The crystallographic basis of this *P*2/*c* setting (**a**, **b**, and **c**) is related to that of the original *P*2/*a* setting (**a**□, **b**□, and **c**□) by the following expressions: **a** = –**a**□ – **c**□; **b** = **b**; and **c** = **a**□. The following description of the α-phase is consistent with the structure in the standard *P*2/*c* format. It should be noted, however, that a non-conventional metric unit cell has been chosen to ensure that the structural features align with the unit cell axes.

Although there are several reported studies of the relative thermodynamic stability and phase equilibria of the $NaAlSiO_4$-$LiAlSiO_4$-SiO_2-H_2O system (Fasshauer et al., 1998; London, 1984; Haussühl et. al., 2012), of which petalite is a key member, there is a lack of accurate high pressure structural and elasticity data for petalite. The objective of this study was to rectify this situation, and herein we report an extensive HP-XRD analysis of petalite and describe in detail a previously undiscovered high-pressure phase of this mineral (β-phase). Furthermore, we have collected precise unit cell data as a function of pressure, and these have enabled us to determine accurate elastic constants for both the low and high-pressure phases of petalite.

Experimental Details

Two HP-XRD experiments were performed with colorless petalite sourced from the Araçuaí pegmatite district, Jequitinhonha Valley, Minas Gerais, Brazil. The first of these conducted with sample 1 allowed for collection of highly accurate and precise unit cell parameters as a function of pressure. These data were employed in the calculation of the elastic constants of α and β-phases. The second petalite crystal (sample 2) was larger than

sample 1 and was used for the measurement of diffraction data for structural analysis. The following experimental details apply to both crystals unless stated otherwise.

A single crystal of petalite (sample 1: $140 \times 160 \times 25\ \mu m^3$, sample 2: $176 \times 313 \times 30\ \mu m^3$) was loaded in to an ETH diamond anvil cell (DAC) (Miletich et al., 2000) fitted with diamonds with culets 600 μm (sample 1) or 650 μm (sample 2) in diameter. The sample chamber was a cavity drilled in a stainless-steel gasket that was fitted within the DAC, and had dimensions of $300 \times 90\ \mu m^2$ (sample 1) or $400 \times 90\ \mu m^2$ (sample 2). In the case of sample 1 a quartz crystal ($60 \times 80 \times 30\ \mu m^3$) was included in the DAC for pressure calibration measurements (Angel et al., 1997). For the experiment with sample 2, a ruby ball was added to the DAC to act as the pressure calibrant (Mao et al., 1978). After initial unit cell determinations at ambient pressure, a 4:1 MeOH:EtOH solvent mixture was added to the DAC to act as the pressure transmitting medium; this particular alcohol mixture is known to remain hydrostatic up to 9.8 GPa (Angel et al., 2007).

Precise unit cell parameters were determined with a Huber diffractometer equipped with an Eulerian cradle and point detector. The instrument was controlled with the SINGLE software (Angel and Finger, 2011). The method employed for the determination of the unit cell parameters was based on the 8-position centering of the sample reflections (King Jr. and Finger, 1979). High-pressure unit cell data for petalite sample 1 were collected over 0–4.5 GPa. When the pressure was raised to *ca*. 5 GPa the crystal disintegrated, possibly due to a phase transition, and the experiment was terminated.

HP-XRD data for structure determinations were collected with sample 2 at room temperature on an Oxford Diffraction Xcalibur II (α-phase data collections) or Xcalibur I

(β-phase data collection) instrument with monochromated Mo-K_α radiation ($\lambda = 0.71073$ Å); these diffractometers are equipped with a point and charge-coupled device (CCD) detectors, respectively. Data were processed with standard instrument software (Agilent Technologies, 2012). Absorption corrections were applied with the ABSORB (Angel, 2005) program, and the data corrected for DAC dips and other statistical anomalies with AVERAGE. All structure solutions and refinements were performed with Olex2 (Dolomanov et al., 2009). The structures of all phases of petalite were solved directly from the high-pressure CCD data by direct methods. Structural refinements were performed on F^2 by full-matrix least-squares refinement techniques. Due to the limited data obtained from the HP-XRD data collections no anisotropic parameters were refined for any of the structural models. Two of the SiO_4 tetrahedra in the structural model of the β-phase were found to be disordered and were modeled accordingly. It was not possible to refine the relative occupancies of the two components of the disorder models so they were fixed to be 50%, and the U_{iso} values of the atoms were fixed to be equal. Where necessary Si–O bond length constraints were applied to the disordered components. Not surprisingly the thermal parameters for the Li^+ ions did not refine to reasonable values. To overcome this issue the U_{iso} values of the two symmetry independent Li^+ ions were constrained to be equal. Table 1 summaries the key crystallographic refinement parameters obtained in this study. HP-XRD data in CIF format for the α-phase [at room pressure, and at 0.32(5), 0.56(5), 0.89(5), and 1.25(5) GPa] and the β-phase [at 2.71(5) GPa] have been deposited with the American Mineralogist Crystal Structure Database.

Results and Discussion

Elastic Constants

Figure 2 shows the evolution of the petalite unit cell volume with increasing pressure and Table 2 lists the unit cell parameters of petalite as a function of pressure. A graphical representation of these data and an F_E *vs.* f_E plot are provided in Figures 3 and 4, respectively. The *P–V* data show the occurrence of two reversible pressure-induced phase transitions, the first at *ca.* 1.5 GPa and the second at *ca.* 2.5 GPa. These transitions are first order in nature, and proceed in the order: α-phase → β′-phase → β-phase, where the β′-phase is an intermediate phase (see section 3.2.2). The overall consequence of the α → β transition is a tripling of the unit cell volume; this is most obvious in the CCD images of the two phases (Fig. 5) in which superlattice reflections are present at $\mathbf{q} = \frac{1}{3}\mathbf{c}^*$ in the diffraction pattern of the β-phase.

The *P–V* data for both the α and β-phases have been fitted, by a least-squares technique, with 3rd order Birch-Murnaghan (BM) equations of state (EoS) (Angel, EOS-FIT). These fits allow for the elucidation of the elastic constants of these two phases, and these are presented in Table 3. However, attention must be given to the estimated standard deviation (esd) values reported with these constants, in particular those for the β-phase, as these are perhaps larger than ideal – this is a consequence of the limited number of available data points to which the EoS functions are fitted. Nonetheless, these constants are notably more accurate and appropriate than those reported by Fasshauer et al. (1998). These authors evaluated the elastic constants for petalite from synchrotron data, yet they did not account for the occurrence of the pressure induced phase transitions and 'cycled' the pressure on the sample, thus forcing the

crystalline sample to pass through these transitions multiple times. It is therefore not surprising that their reported values for the elastic constants of petalite (Table 3) differ from those determined in this study. However, our experimentally determined value of K_0 for the α-phase of petalite is in excellent agreement with value reported by Haussühl et al. (2012), 49(1) GPa, that was derived from density functional theory (DFT) calculations based on elastic stiffness coefficients determined by resonant ultrasound spectroscopy (RUS) measurements conducted under ambient conditions (*i.e.* with α-phase petalite samples). Yet, these authors also reported DFT calculations of the petalite unit cell volume as a function of pressure (up to 30 GPa) that also failed to identify the $\alpha \rightarrow \beta' \rightarrow \beta$ phase transitions.

Table 4 lists elastic constants for selected tetrahedral framework minerals and layered silicates for comparison with petalite. It is apparent that the bulk modulus of the α-phase of petalite is slightly more compressible than the alkali feldspars and slightly less compressible than the alkali feldspathoids. In contrast, the bulk modulus of the β-phase of petalite is more akin to those of quartz and the archetypical layered silicate talc in which the SiO_4 layers are not pillared in the third dimension by either AlO_4 or AlO_6 polyhedra, and with pyrophyllite that comprises stacked aluminosilicate layers that are also not covalently linked *via* bridging polyhedra. This would suggest that the presence of the AlO_4 tetrahedra that interconnect the SiO_4 double sheets (Fig. 1) has a minimal impact on the ability of the petalite framework to withstand pressure.

It would be constructive to quantify the compressibilities (β_i) of the three crystallographic axes from the unit cell length *vs.* pressure data for petalite (Fig. 3). For an orthogonal unit cell ($\alpha = \beta = \gamma = 90^o$) a reasonable approximation of a β_i value can be

obtained by fitting the axis length *vs.* pressure data with an appropriate BM EoS and from the axial bulk modulus (K_i) β_i can be estimated with the equation $\beta_i = (3K_i)^{-1}$. However, this approximation assumes that the strain tensor is restricted, by symmetry, from rotating. Yet, in the case of a monoclinic system one of the three unit cell angles is free to change, thus the requisite symmetry constraints for this approximation are violated. Indeed, to evaluate the axial compressibilities for a non-orthogonal unit cell it is necessary to calculate the full strain tensor, yet due to the limited number of data points available for α and β-phases of petalite such calculations are not feasible.

High pressure structural analysis

α-phase compression mechanism. To aid in the interpretation of the structural changes experienced by the α-phase in response to pressure, it is beneficial to first ascertain the degree of distortion exhibited by the polyhedra comprising the petalite framework. Such distortion of the individual cation tetrahedra can be estimated from the tetrahedral angular variance (σ_{tet}) and quadratic elongation ($\langle\lambda_{tet}\rangle$) parameters (Robinson et al., 1971). These distortion parameters for the AlO_4, SiO_4, and LiO_4 polyhedra within the α-phase of petalite are listed in Table 5 as a function of pressure. Also included in this table are the volumes of the polyhedra (V_{poly}) and the center-to-vertex distance (l_0) for a geometrically ideal tetrahedron ($\sigma_{tet} = 0$, $\langle\lambda_{tet}\rangle = 1$) with a volume equal to that of the distorted polyhedron. It is evident that after an initial adjustment to the applied pressure the nearly geometrically ideal SiO_4 tetrahedra remain unaltered with increasing pressure; this finding is also reflected in the lack of statistically significant pressure-induced changes in the bond lengths and angles associated with these tetrahedra (Table 6). Consequently, the SiO_4 tetrahedra can be treated as rigid units, at least over the pressure

range investigated (< 5 GPa). Unlike the SiO_4 tetrahedra, the AlO_4 tetrahedra are greatly distorted, but the σ_{tet} values for this unit are suggestive, but not conclusive, of an overall small reduction in the degree of distortion of these polyhedra with increasing pressure.

A rigid unit approximation cannot be extended to the LiO_4 units. These polyhedra are best considered as possessing geometries that are intermediate between those of an idealized tetrahedron ($\sigma_{tet} = 0$) and a perfect square planar arrangement ($\sigma_{tet} = 47.886$). The variation in the elongation parameter, $<\lambda_{tet}>$, of the LiO_4 polyhedra with pressure is negligible, indicating that there is virtually no change with pressure in the deviation of the Li–O bond lengths from their optimum length (l_0) at that specific pressure. This implies that any pressure-induced distortions of the LiO_4 polyhedra must be facilitated by adjustments in the O–Li–O angles rather than by disproportionate changes in the Li–O bond lengths. This conclusion is further supported by the decrease in the σ_{tet} parameter with increasing pressure that signifies a reduction in angular distortion of the LiO_4 unit as it tends towards a more regular tetrahedral arrangement with increasing pressure.

As discussed in section 3.1, the bulk modulus of the α-phase is similar to that of silicate minerals composed of either silicate or aluminosilicate layers that are not covalently linked in the third dimension. This result would suggest that the AlO_4 tetrahedra play a minor role in the compression mechanism of this phase. Consequently, one must expect, perhaps counter-intuitively, that compression of the structure is enabled by changes within the silicate double-layers. Further support for this hypothesis is provided by the percentage decreases in the unit cell axes over the 0–1.5 GPa range: ~0.9% (*a*-axis), ~1.6% (*b*-axis), and ~1.4% (*c*-axis). These values indicate that

compression within the silicate layers parallel to the (100) plane is favored over compression in the [100] direction that lies ~51° from the a^*-axis.

To aid in the evaluation of the pressure response of the α-phase, the structure of the silicate double-layers can be simplified by applying the rigid unit approximation to the SiO_4 tetrahedra. Furthermore, as oxygen atom O3 resides on an inversion centre (2*d*) the compressional mechanism must not incorporate any change in the Si1–O3–Si1^{viii} bond angle, or rotation of the connected $(Si1)O_4$ tetrahedra relative to each other. This second symmetry constraint also applies to the connected $(Si2)O_4$ tetrahedra because the bridging oxygen atom O5 is located on a 2-fold axis (2*f*). Fortuitously, although there are no symmetry restrictions on the Si2–O5–Si2^{ix} bond angle, there is no statistically relevant change in this angle with pressure (Table 6). Consequently the Si_2O_7 units, which are shown as light grey and purple in Figure 6, may also be treated as rigid entities. Therefore the compression mechanism must be due primarily to tilting and/or rotation of these Si_2O_7 units relative to each other.

The 'pivot points' for these possible motions are atoms O1, O2, O4 and O6, thus to evaluate the behavior of the structure it is necessary to assess changes to the bond angles involving these atoms (Table 6). The O1···O4···O2^{i} and O4···O2^{i}···O1^{i} angles represent the hinges for the corner sharing Si_2O_7 units, and they increase and decrease with increasing pressure, respectively (Table 6). Moreover, the Si1^{i}–O2^{i}–Si2 (symmetry equivalent to the Si1–O2–Si2^{vii} angle in Table 6) and Si1–O4–Si2 angles decrease with increasing pressure. It is the concerted changes in these angles with increasing pressure that allows for contraction of the structure along the crystallographic *b*-axis. The concomitant opening of the Si2–O6–Al1 (symmetry equivalent angle Si2^{ix}–O6^{ix}–Al1^{x}

shown in Fig. 6) hinge permits compression along the *c*-axis and an overall reduction in the β-angle.

The ultimate consequence that can be envisaged as a result of these concerted hinge motions is movement of Si_2O_7 units relative to each other such that there is subtle lessening in the corrugation of the double-layers. This in turn will result in a small decrease in the length of the *a*-axis in response to pressure, exactly as observed in the experimental data (Fig. 3).

Unfortunately, the estimated standard deviation values associated with the bond lengths and angles involving the Li^+ ion are too high to allow for a conclusive determination of the mechanism that causes a reduction in the LiO_4 polyhedral distortion with increasing pressure. However, the data do suggest that the principal driving force for the decrease in distortion is facilitated by the movement of the $(Si2)_2O_7$ units, as evidenced by the decrease in the Si2–O6–Li1 angle with increasing pressure and the absence of changes in the Li1–O1–Si1 angles.

Crystal structure of the β-phase. At *ca*. 1.5 GPa the compression mechanism for the α-phase reaches a limiting point and the crystal undergoes a first-order phase transition to an immediate phase denoted herein as the β′-phase. The quality of the diffraction data for this phase precluded determination of its crystal structure, but it is likely to be a composite phase comprising structural features associated with both the α and β-phases, but given the unit cell parameters for this phase it is probably most akin to the structure of the β-phase, and may possibly be an incommensurate phase. At *ca*. 2.5 GPa the crystal fully converts to the β-phase.

Given that the compression mechanism of the α-phase is enabled by the rigid motion of the Si_2O_7 units, one may reasonably expect that once this mechanism reaches its limiting point that the subsequent phase transition would incorporate an increase in the conformational freedom of these units, perhaps *via* breaking of the inversion and 2-fold symmetries of the $(Si1)_2O_7$ and $(Si2)_2O_7$ units. Therefore, the expected candidate space groups for the β-phase would be the monoclinic translationengleiche subgroups (*t* subgroups) of *P*2/*c*, *P*2 and *Pc*. Yet, the klassengleiche index (*k*-index) for this first-order transition equals three and this precludes the β-phase belonging to a *t* subgroup of *P*2/*c*. In fact, the α → β transition is isomorphic with only ⅔ of the Si_2O_7 units exhibiting a reduction in symmetry *i.e.* tilting/rotation of the SiO_4 units relative to each other (Fig. 7a).

Unfortunately, because of the disorder exhibited by two of the six symmetry independent SiO_4 tetrahedra, which also impact the geometries of the AlO_4 and LiO_4 polyhedra, a comparative analysis of the tetrahedral distortion parameters for the cation polyhedra would be redundant. Furthermore, a detailed discussion of the variations in the construction of the four unique Si_2O_7 units (color coded in Fig. 7) is also of questionable value. However, we can assess the broader structural differences between the two petalite phases. The framework of the β-phase comprises structural features that are essentially analogous to those observed in the crystal structure of the α-phase (Fig. 1), namely silicate double layers pillared by AlO_4 tetrahedra. Yet, there are significant adaptations to the internal structure of the silicate layers in the β-phase caused by the distortion in ⅔ of the Si_2O_7 units. An overlay of the crystal structures of the α- and β-phases (Fig. 8) shows that the major consequence of this internal rearrangement of the silicate layers is the

creation of two types of interlayer channels (denoted A and B in Fig. 8) with dimensions notably different from the channels in the α-phase that are all symmetry related. At 1.25(5) GPa the cross-sections of the channels in the α-phase are *ca*. 3.24 × 4.01 $Å^2$; for the β-phase at 2.71(5) GPa the A channels are *ca*. 2.61× 4.14 $Å^2$ and the cross-sections of the B channels are *ca*. 4.42 × 2.64 $Å^2$. These cross-sectional dimensions are only approximations, but they do show that by converting the dimensions of the channels during the phase transition the petalite structure is able to accommodate contraction along the [001] direction. This transition is also accompanied by a small reduction in the interlayer distance of *ca.* 0.2 Å. However, there do not appear to be any significant differences in the coordination environments of the Li cations in the two phases.

Implications

This high-pressure single-crystal XRD study of petalite has revealed, for the first time, that petalite undergoes two first-order phase transitions within the 0–4.5 GPa pressure range. The transformation of the low-pressure α-phase to the high-pressure β-phase proceeds via an intermediate phase, β′-phase, of unknown structure. The α and β-phases are structurally similar although there are small differences in the construction of the silicate double-layers. The compression mechanism of the α-phase has also been elucidated and it has been shown that the rigid body movement of the Si_2O_7 units comprising the silicate double-layers is responsible for the compression of the structure. It is of note that these modifications within the silicate layers lead to a reduction in the distortion of the LiO_4 polyhedra with increasing pressure. This is also one of the first

studies that provides details of how Li in 4-fold coordination with oxygen responds to pressure.

The bulk moduli of the α- and β-phases are 49(1) and 35(3) GPa, respectively, showing that the high-pressure phase (β) is more compressible than the low-pressure phase (α). The bulk modulus for α is slightly lower than those reported for tetrahedral frameworks such as the alkali feldspars and slightly greater than those reported for alkali feldspathoids. The lower bulk modulus of the β-phase, however, is closer in magnitude to values reported for layered silicates such as talc and pyrophyllite. The results of this study therefore enhance our understanding of the effect of composition and mechanisms that control the compression of tetrahedral framework structures.

Acknowledgments

N.L.R., E.C.S, and J.Z. gratefully acknowledge support for this work from the National Science Foundation through grant EAR-1118691 and support from the College of Science at Virginia Tech. The XCalibur2 instrument employed in this study was purchased through the NSF grant CHE-0131128. Research conducted at Oak Ridge National Laboratory was sponsored by the Scientific User Facilities Division, Office of Basic Energy Sciences, U.S. Department of Energy.

References

Agilent Technologies: Data collection and processing software, CrysAlisPro (version 171.36), Agilent Technologies (2012).

Angel, R. J.: All EoS fits to the data presented herein were performed with EOS-FIT (version 5.2), which is available at www.rossangel.net.

Angel R. J. (2005) Absorption corrections for diamond-anvil pressure cells implemented in the software package Absorb6.0. Journal of Applied Crystallography, 37, 486-492.

Angel R. J., and Finger, L. W. (2011) SINGLE: a program to control single-crystal diffractometers. Journal of Applied Crystallography, 44, 247–251.

Angel, R. J., Bujak, M., Zhao, J., Gatta, G.D., and Jacobsen, S. D. (2007) Effective hydrostatic limits of pressure media for high-pressure crystallographic studies. Journal of Applied Crystallography, 40, 26–32.

Angel, R. J., Allan, D. R., Miletich, R., and Finger, L. W. (1997) The use of quartz as an internal pressure standard in high-pressure crystallography. Journal of Applied Crystallography, 30, 461–466.

Benusa, M., Angel, R.J., Ross, N.L. (2005) Compression of albite, $NaAlSi_3O_8$. American Mineralogist, 90, 1115-1120.

Černý, P., London, D. (1983) Crystal chemistry and stability of petalite. Tschermaks Mineralogische und Petrographische Mitteilungen, 31, 81–96.

Dolomanov, O. V., Bourhis, L. J., Gildea, R. J., Howard, J. A. K., and Puschmann, H. (2009) OLEX2: a complete structure solution , refinement and analysis program. Journal of Applied Crystallography, 42, 339–341.

Fasshauser, D.W., Chatterjee, N. D., and Cemic, L. (1998) A thermodynamic analysis of the system $NaAlSiO_4$-$LiAlSiO_4$-SiO_2-H_2O system based on new heat capacity, thermal expansion, and compressibility data for selected phases. Contributions to Mineralogy and Petrology, 133, 186–198.

Gatta, G.D., and Angel, R.J. (2007) Elastic behavior and pressure-induced structural evolution of nepheline: Implications for the nature of the modulated superstructure. American Mineralogist, 92, 1446-1455.

Gatta, G.D., Rotiroti, N., Boffa Ballaran, T., and Pavese, A. (2008) Leucite at high pressure: Elastic behavior, phase stability, and petrological implications. American Mineralogist, 93, 1588-1596.

Haussühl, E., Schreuer, J., Winkler, B., Haussühl, S., Bayarjargal, L., and Milman, V.(2012) Structure-property relations and thermodynamic properties of monoclinic petalite, $LiAlSi_4O_{10}$. Journal of Physics: Condensed Matter, 24, 345402.

King Jr., H. E., and Finger, L. W. (1979) Diffracted beam crystal centering and its application to high-pressure crystallography. Journal of Applied Crystallography, 12, 374–378.

London, D. (1984) Experimental phase equilibria in the $LiAlSiO_4$-SiO_2-H_2O: a petrogenetic grid for lithium-rich pegmatites. American Mineralogy, 69, 995–1004.

Mao, H. K., Bell, P. M., Shaner, J. W., and Steinberg, D. J. (1978) Specific volume measurements of Cu, Mo, Pd, and Ag and calibration of the ruby R_1 fluorescence pressure gauge from 0.06 to 1 Mbar. J. Applied Physics, 49, 3276–3283.

McCarthy, A. C., Downs, R. T., and Thompson, R. M. (2008) Compressibility trends of the clinopyroxenes, and in-situ high-pressure single-crystal X-ray diffraction study of jadite. American Mineralogy, 93, 198–209.

Miletich, R., Allan, D. R., and Kuhs, W. F. (2000) High-Temperature and High-Pressure Crystal Chemistry, Mineralogical Society of America Geochemical Society (Vol.41), R. M. Hazen and R. T. Downs (Eds.), pg. 445–519.

Pawley, A. R., Clark, S. M., and Chinnery, N. J. (2002) Equation of state measurements of chlorite, pyrophyllite, and talc. American Mineralogy, 87, 1172–1182.

Robinson, K., Gibbs, G. V., and Ribbe, P. H. (1971) Quadratic elongation: a quantitative measure of distortion in coordination polyhedra. Science, 172, 567–570.

Tagai, T., Reid, H., Joswig, W., and Korekawa, M. (1981) Kristallographische untersuchungen eines petalits mittels neutronenbeugung und transmissionselektronenmikroskopie. Zeitschrift für Kristallographie, 160, 159–170.

Figure Captions

Figure 1. The crystal structure of the low-pressure α-phase of petalite in the *P*2/*c* setting: (a) view along the [010] direction; (b) view along the [001] direction. Light and dark purple tetrahedra represent symmetry independent SiO_4 units, blue tetrahedra are associated with AlO_4 units, and the orange spheres represent Li^+ ions that reside within the cavities of the anionic $AlSi_4O_{10}$ framework.

Figure 2. *V–P* data for petalite: data collected with two different petalite samples are shown as solid (sample 1) and open circles (sample 2). Error bars have been included but are smaller than the symbols. Solid black curves represent 3rd order BM-EoS fits to the *V–P* data [$w\chi^2 = 0.8215$, α-phase, 0–1.5 GPa; $w\chi^2 = 2.4719$, β-phase, 2.5–4.5 GPa]. The β-phase volume has been divided by three to normalize it with respect to the volume of the α-phase.

Figure 3. Petalite unit cell parameters as a function of pressure: (A) axes lengths [circles: *a*-axis; squares: *b*-axis; diamonds: *c*-axis]; (B) β-angle. The β-phase *c*-axis length has been divided by three to normalize it with respect to the length of the α-phase *c*-axis.

Figure 4. F_e *vs.* f_e plot for petalite calculated from accurate and precise unit cell data determined from eight-position centering of selected sample reflections (see section 3.1 in the manuscript).

Figure 5. 0*kl* projections of the HP-XRD data recorded with a CCD detector: (left) α-phase (ambient pressure); (right) β-phase at 2.71(5) GPa.

Figure 6. Section of the silicate double-layer within the structure of the α-phase of petalite showing atom labels. Symmetry codes: (i) x, $1 + y$, z; (viii) $1 - x$, $-y$, $2 - z$; (ix) $1 - x$, y, $^3/_2 - z$; (x) x, y, $1 + z$.

Figure 7. The crystal structure of the high-pressure β-phase of petalite in the *P*2/*c* setting: (a) view along the [010] direction; (b) view along the [001] direction. Light and dark purple and brown polyhedra represent symmetry independent Si_2O_7 units. Dark blue tetrahedra are AlO_4 units, and orange spheres represent Li^+ cations. For clarity, in the case of disordered SiO_4 units only a single component is shown.

Figure 8. Overlay of the α-phase (light grey) and β-phase (multicoloured) of petalite. The letters A and B denote the two symmetry independent cavities observed in the β-phase; only symmetry equivalent cavities are present in the crystal structure of the α-phase; Li^+ cations of this phase have been omitted for clarity. Note: these are exact overlays; no corrections for variations in the unit cell parameters of the two phases have been made. Dotted lines represent outlines of the unit cells. The red and green lines represent the *x* and *y* dimensions, respectively, used to measure the cross-sections of the channels.

440
441
442 **Table 1.** Refinement details for petalite as a function of pressure.

	Pressure (GPa)					
	Ambient	**0.32(5)**	**0.56(5)**	**0.89(5)**	**1.25(5)**	**2.71(5)**
Phase	α-phase	α-phase	α-phase	α-phase	α-phase	β-phase
Crystal system	Monoclinic	Monoclinic	Monoclinic	Monoclinic	Monoclinic	Monoclinic
Space group	*P*2/*c*	*P*2/*c*	*P*2/*c*	*P*2/*c*	*P*2/*c*	*P*2/*c*
Z	2	2	2	2	2	6
a (Å)	11.2296(1)	11.2067(4)	11.1895(4)	11.1705(4)	11.1425(4)	10.830(1)
b(Å)	5.1396(3)	5.1228(4)	5.1100(4)	5.0963(4)	5.0723(4)	5.0530(3)
c (Å)	11.7514(5)	11.7160(7)	11.6872(7)	11.6569(7)	11.6092(7)	33.59(2)
β angle (^{o})	141.312(1)	141.243(2)	141.190(2)	141.134(2)	141.074(2)	140.6648(2)
V (Å^3)	423.95(3)	421.07(4)	418.83(4)	416.41(4)	412.26(4)	1165.2(7)
ρ_{cal} (g cm^{-3})	2.399	2.416	2.429	2.443	2.467	2.619
Unique reflns. (I >2σI)	398	283	449	451	429	885
R(int)	0.037	0.098	0.043	0.040	0.045	0.111
Nº parameters	32	32	32	32	32	106
Nº restraints	0	0	0	0	0	0
GoF	1.193	1.203	1.125	1.171	1.154	1.586
$R1$ (I >2σI)	0.0484	0.0456	0.0494	0.0513	0.0593	0.0955
$wR2$ (I >2σI)	0.1056	0.0999	0.1133	0.1181	0.1288	0.1748

443
444

445
446
447 **Table 2**. Unit cell parameters for petalite as a function of pressure. Data are listed in the
448 order in which they were measured. The β-phase *c*-axis length has been divided by three
449 to normalize it with respect to the length of the α-phase *c*-axis.
450

Pressure (GPa)	*a*-axis (Å)	*b*-axis (Å)	*c*-axis (Å)	β angle	Volume (Å^3)
Sample 1					
0.000(7)	11.22860(3)	5.1385(1)	11.7486(2)	141.311(3)	423.74(4)
0.343(6)	11.20328(9)	5.1194(2)	11.7096(5)	141.239(3)	420.47(5)
0.355(7)	11.20553(4)	5.11908(9)	11.7091(2)	141.240(3)	420.50(4)
0.670(7)	11.18278(7)	5.1023(1)	11.6730(3)	141.171(4)	417.60(5)
1.041(7)	11.1547(1)	5.0822(9)	11.6290(2)	141.094(3)	414.06(4)
1.472(7)	11.12857(9)	5.0556(1)	11.5803(3)	141.076(4)	409.35(5)
2.038(8)	10.9432(2)	5.0512(2)	11.3745(3)	140.836(4)	397.08(5)
2.639(8)	10.8334(6)	5.0444(2)	11.1830(3)	140.738(4)	386.77(6)
3.33(1)	10.7221(4)	5.0348(2)	11.0256(4)	140.512(6)	378.49(4)
3.782(9)	10.6409(2)	5.0346(2)	10.9077(4)	140.302(5)	373.25(6)
4.35(1)	10.5284(2)	5.0346(2)	10.7402(4)	139.992(6)	366.00(7)
Sample 2					
0.00	11.2296(1)	5.1396(3)	11.7514(5)	141.312(1)	423.96(5)
0.32(5)	11.2067(2)	5.1228(4)	11.7160(7)	141.243(3)	421.07(7)
0.56(5)	11.1895(2)	5.1100(5)	11.6872(7)	141.190(3)	418.83(7)
0.89(5)	11.1705(3)	5.0963(4)	11.6569(8)	141.134(3)	416.41(8)
1.25(5)	11.1425(2)	5.0723(5)	11.6092(9)	141.074(3)	412.26(9)
2.07(5)	10.9342(1)	5.0507(4)	11.3647(7)	140.816(3)	396.54(7)
2.21(5)	10.9301(2)	5.0504(4)	11.3588(6)	140.809(3)	396.22(7)
2.59(5)	10.9028(3)	5.0472(4)	11.3240(7)	140.772(3)	394.082(7)
1.39(5)	11.1379(1)	5.0661(3)	11.5978(5)	141.076(1)	411.16(5)
1.69(5)	10.98981(7)	5.0571(2)	11.4321(4)	140.897(1)	400.73(4)
1.91(5)	10.93681(7)	5.0511(3)	11.3659(6)	140.826(1)	396.62(5)
2.09(5)	10.9332(2)	5.0510(6)	11.361(1)	140.825(3)	396.3(1)

451
452

453 **Table 3.** Experimentally Determined Elastic Constants for the α and β-phases of petalite.
454

Parameter	α-phase	β-phase	Fasshauer et al.[†]
K_0 (GPa)	49(1)	35(3)	33
K'	–6(1)	0.0(6)	0.1
K'' (GPa^{-1})	–2.07	–0.45	–

455 [†]Fasshauer et al. (1998). No esd values were reported for these values.
456

457 **Table 4.** Equation of state parameters of other minerals for comparison with petalite.
458

Mineral	Formula	K_0 (GPa)	K' / K'' (GPa^{-1})	Reference
Albite	$NaAl_3SiO_8$	52.3(9)	8.8(6)/-2.8(2)	Benusa et al. (2005)
Microcline	$KAlSi_3O_8$	58.7(7)	3.8(5)/-0.95(17)	Ross (personal comm.)
Leucite (tetragonal) Leucite (triclinic)	$KAlSi_2O_6$	41.9(6) 33.2(5)	4 (fixed) 4 (fixed)	Gatta et al. (2008)
Nepheline	$NaAlSiO_4$	47.32(26)	2.77(24)/0.758(79)	Gatta and Angel (2007)
Pyrophyllite	$Al_2Si_4O_{10}(OH)_2$	37(3)	10(1)	McCarthy et al. (2008)
Talc	$Mg_3Si_4O_{10}(OH)_2$	41(4)	6(2)	Pawley et al. (2002)
Quartz	SiO_2	37.12(4)	5.99(4)	Angel et al. (1997)

459
460
461

Table 5. Distortion parameters for polyhedra in the α-phase of petalite.

Parameter		Pressure (GPa)				
		Ambient	**0.32(5)**	**0.56(5)**	**0.89(5)**	**1.25(5)**
Si1	σ_{tet} (°)	1.336	1.589	1.499	1.491	1.381
	V_{poly} (Å^3)	2.139	2.142	2.145	2.126	2.123
	l_0 (Å)	1.609	1.610	1.611	1.606	1.605
	$\langle\lambda_{tet}\rangle$	1.001	1.000	1.001	1.001	1.001
Si2	σ_{tet} (°)	1.344	1.726	1.540	1.556	1.667
	V_{poly} (Å^3)	2.115	2.114	2.116	2.112	2.097
	l_0 (Å)	1.603	1.603	1.604	1.603	1.599
	$\langle\lambda_{tet}\rangle$	1.001	1.001	1.000	1.000	1.001
Al1	σ_{tet} (°)	9.134	9.457	9.424	9.342	9.211
	V_{poly} (Å^3)	2.553	2.546	2.525	2.552	2.538
	l_0 (Å)	1.707	1.706	1.701	1.707	1.704
	$\langle\lambda_{tet}\rangle$	1.021	1.022	1.022	1.022	1.021
Li1	σ_{tet} (°)	20.235	19.982	19.961	19.535	19.273
	V_{poly} (Å^3)	3.251	3.195	3.173	3.184	3.159
	l_0 (Å)	1.851	1.840	1.835	1.838	1.833
	$\langle\lambda_{tet}\rangle$	1.100	1.097	1.098	1.093	1.091

Table 6. Selected bond lengths (Å) and angles (o) for the α-phase of petalite as a function of pressure. Parameters that exhibit statistically significant changes with pressure are highlighted in grey.

	Pressure (GPa)				
	Ambient	**0.32(5)**	**0.56(5)**	**0.89(5)**	**1.25(5)**
Si1–O1	1.607(10)	1.605(12)	1.618(11)	1.600(11)	1.599(14)
Si1–O2	1.608(6)	1.619(5)	1.615(5)	1.613(5)	1.614(7)
Si1–O3	1.602(2)	1.601(3)	1.596(2)	1.596(2)	1.591(3)
Si1–O4	1.622(4)	1.616(4)	1.617(4)	1.617(4)	1.619(6)
Si2–O2^{i}	1.615(5)	1.607(4)	1.612(4)	1.611(4)	1.611(6)
Si2–O4	1.600(7)	1.608(7)	1.610(7)	1.605(7)	1.596(9)
Si2–O5	1.599(4)	1.594(4)	1.594(4)	1.598(4)	1.597(5)
Si2–O6	1.600(4)	1.606(5)	1.599(4)	1.599(4)	1.594(5)
Al1–O1^{ii}	1.716(8)	1.717(9)	1.709(8)	1.723(9)	1.718(11)
Al1–O1^{iii}	1.716(8)	1.717(9)	1.709(8)	1.723(9)	1.718(11)
Al1–O6	1.733(4)	1.732(4)	1.730(4)	1.728(4)	1.725(5)
Al1–O6^{iv}	1.733(4)	1.732(4)	1.730(4)	1.728(4)	1.725(5)
Li1–O1^{v}	1.931(12)	1.905(15)	1.913(13)	1.933(14)	1.910(17)
Li1–O1^{vi}	1.931(12)	1.905(15)	1.913(13)	1.933(14)	1.910(17)
Li1–O6	1.952(11)	1.949(12)	1.933(11)	1.910(12)	1.919(14)
Li1–O6^{iv}	1.952(11)	1.949(12)	1.933(11)	1.910(12)	1.919(14)
Al1···Li1	2.578(14)	2.592(17)	2.559(14)	2.529(16)	2.541(19)
Al1···Li1^{vii}	2.562(14)	2.531(17)	2.551(14)	2.568(16)	2.532(19)
O1–Si1–O2	110.9(4)	111.7(4)	111.2(3)	111.3(4)	111.3(4)
O1–Si1–O3	110.97(17)	110.89(19)	110.83(17)	110.75(18)	110.7(2)
O1–Si1–O4	107.7(4)	107.5(4)	107.0(4)	107.1(4)	107.4(5)
O2–Si1–O3	109.2(3)	108.7(3)	109.1(3)	109.1(3)	109.0(4)
O2–Si1–O4	109.7(3)	109.6(3)	109.6(3)	109.7(3)	109.3(4)
O3–Si1–O4	108.3(3)	108.4(3)	109.1(2)	108.9(3)	109.1(3)
O2^{i}–Si2–O4	109.9(4)	110.3(4)	109.9(4)	110.3(4)	110.4(5)
O2^{i}–Si2–O5	110.6(4)	110.6(4)	110.7(4)	110.4(4)	110.5(5)
O2^{i}–Si2–O6	107.6(2)	106.9(2)	107.0(2)	107.2(2)	106.9(3)
O4–Si2–O5	108.0(3)	107.7(3)	108.2(3)	107.9(3)	107.8(4)
O4–Si2–O6	110.7(4)	110.2(4)	110.1(3)	111.1(4)	110.7(5)
O5–Si2–O6	110.1(4)	111.1(5)	110.9(4)	110.0(4)	110.5(6)
O1^{ii}–Al1–O1^{iii}	97.8(5)	97.6(5)	97.2(5)	97.7(5)	97.9(6)
O1^{ii}–Al1–O6	117.3(3)	116.9(3)	117.2(3)	117.6(3)	117.2(4)
O1^{ii}–Al1–O6^{iv}	113.7(3)	114.6(4)	114.2(3)	113.6(4)	113.9(4)
O1^{iii}–Al1–O6	113.7(3)	114.6(4)	114.2(3)	113.6(4)	113.9(4)
O1^{iii}–Al1–O6^{iv}	117.3(3)	116.9(3)	117.2(3)	117.6(3)	117.2(4)
O6–Al1–O6^{iv}	98.4(3)	97.5(3)	98.1(2)	98.0(3)	98.0(3)
O1^{v}–Li1–O1^{vi}	84.1(7)	85.4(8)	84.2(7)	84.3(8)	85.4(9)
O1^{v}–Li1–O6	124.9(3)	124.2(3)	124.4(3)	124.6(3)	124.1(3)
O1^{v}–Li1–O6^{iv}	121.8(3)	122.2(4)	121.9(3)	121.1(3)	121.2(4)
O1^{vi}–Li1–O6	121.8(3)	122.2(4)	121.9(3)	121.1(3)	121.2(4)
O1^{vi}–Li1–O6^{iv}	124.9(3)	124.2(3)	124.4(3)	124.6(3)	124.1(3)
O6–Li1–O6^{iv}	84.5(6)	83.8(7)	85.0(6)	86.1(7)	85.5(8)
Si1–O1–Al1^{ii}	147.8(4)	148.0(4)	148.1(4)	148.6(4)	149.2(5)
Si1–O2–Si2^{vii}	152.1(3)	150.2(3)	149.0(3)	147.8(3)	146.0(4)
Si1–O3–Si1^{viii}	180	180	180	180	180
Si1–O4–Si2	148.9(6)	147.8(6)	146.2(6)	145.8(6)	144.9(8)
Si2–O5–Si2^{ix}	163.1(5)	162.1(4)	162.1(4)	162.3(5)	161.8(6)
Si2–O6–Al1	145.1(2)	145.3(2)	146.1(2)	146.4(2)	147.1(3)
Si2–O6–Li1	126.0(3)	125.3(4)	125.3(3)	125.4(4)	124.5(5)
Al1–O1^{ii}–Li1^{v}	89.1(5)	88.5(6)	89.3(5)	89.0(6)	88.4(7)
Al1–O6–Li1	88.6(3)	89.3(4)	88.5(3)	87.9(4)	88.2(4)
Al1–O6^{v}–Li1	88.6(3)	89.3(4)	88.5(3)	87.9(4)	88.2(4)
Li1–O1^{v}–Si1^{v}	123.0(4)	123.4(4)	122.5(4)	122.3(4)	122.3(5)
Li1–O1^{vi}–Si1^{vi}	123.0(4)	123.4(4)	122.5(4)	122.3(4)	122.3(5)
Li1–O6^{vi}–Si2^{iv}	126.0(3)	125.3(4)	125.3(3)	125.4(4)	124.5(5)
O1···O4···O2^{i}	144.1(4)	145.6(4)	146.5(4)	147.3(5)	148.3(6)
O4···O2^{i}···O1^{i}	95.7(3)	94.0(3)	93.0(3)	92.3(3)	90.9(4)

Symmetry codes: (i) $x, 1+y, z$; (ii) $-x, -y, 1-z$; (iii) $x, -y, z-\frac{1}{2}$; (iv) $-x, y, \frac{1}{2}-z$; (v) $-x, 1-y, 1-z$; (vi) $x, 1-y, z-\frac{1}{2}$; (vii) $x, y-1, z$; (viii) $1-x, -y, 2-z$; (ix) $1-x, y, \frac{3}{2}-z$; (x) $x, y, 1+z$

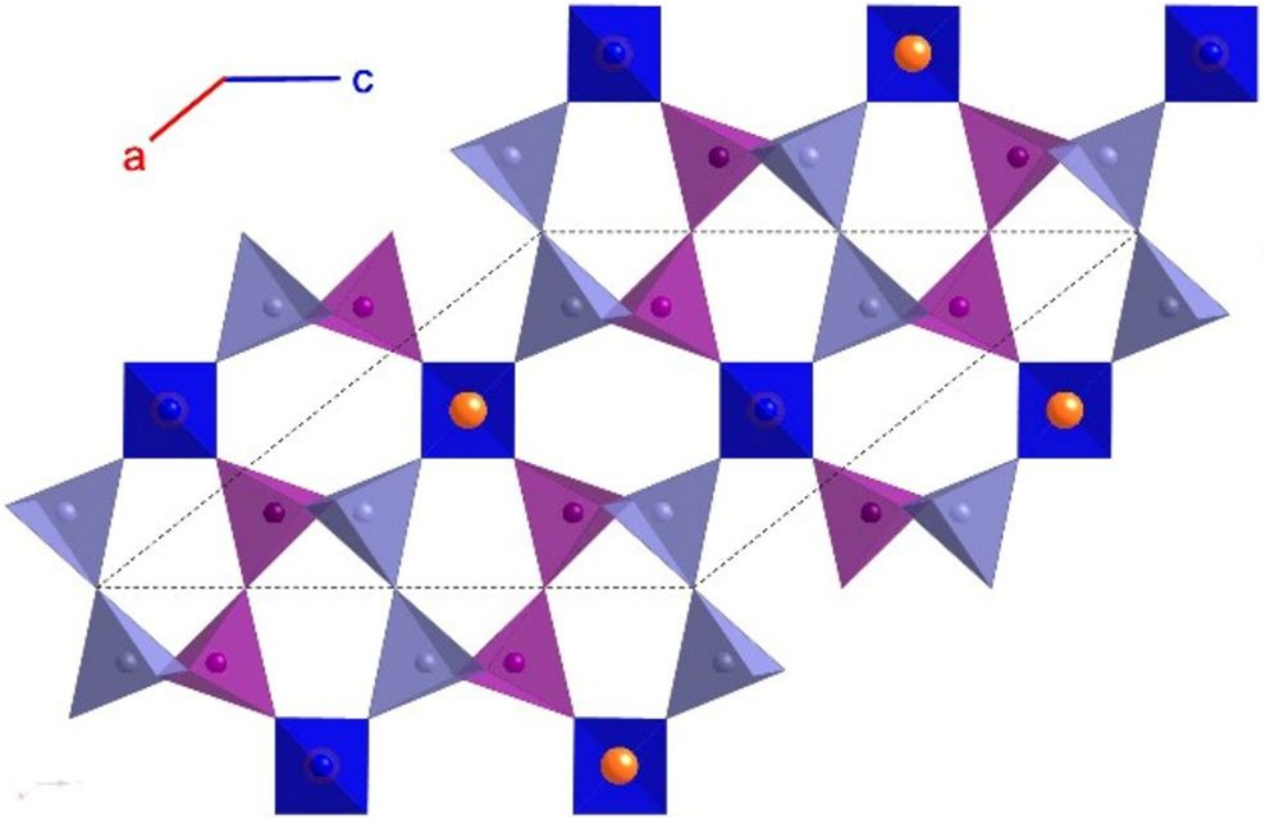

(a)

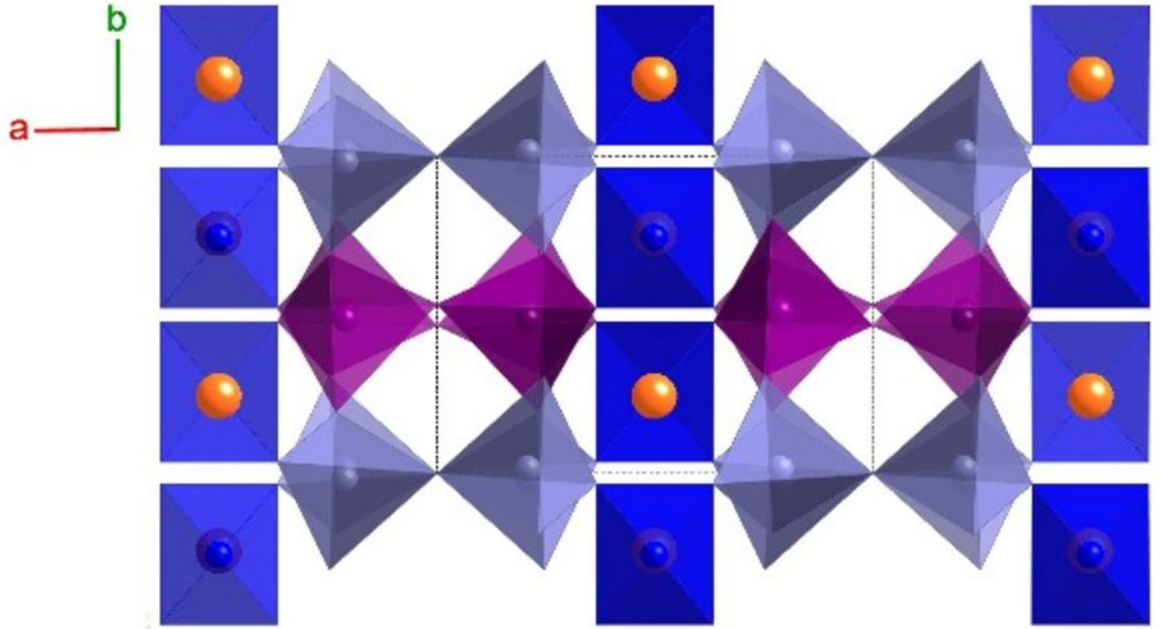

(b)

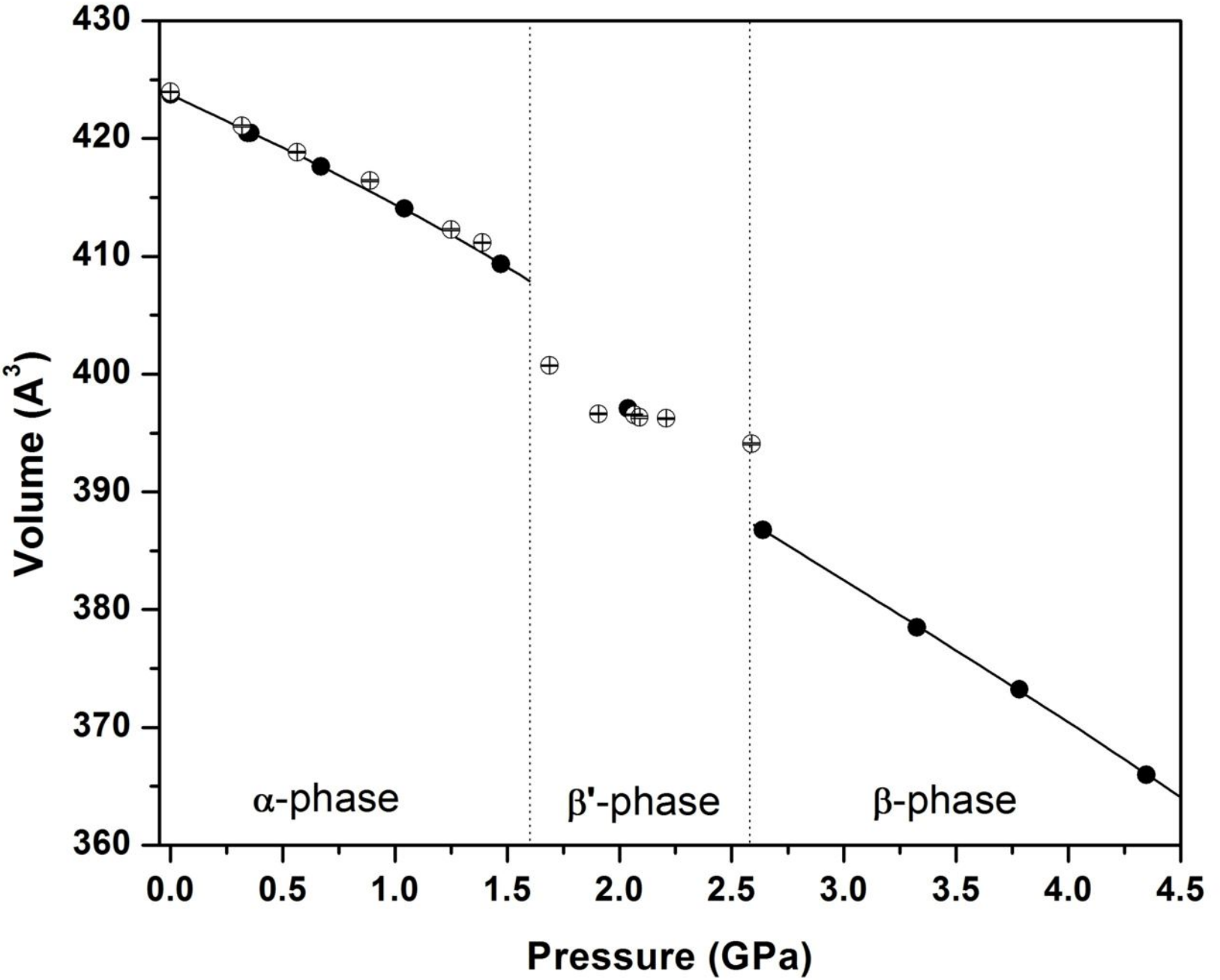
430
420
410
400
390
380
370
360
Volume (A3)
α-phase
β'-phase
β-phase
0.0
0.5
1.0
1.5
2.0
2.5
3.0
3.5
4.0
4.5
Pressure (GPa)

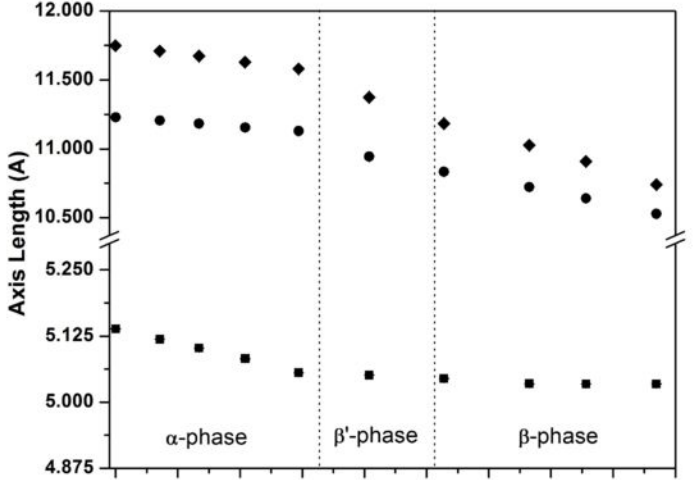
12.000
11.500
11.000
10.500
5.250
5.125
5.000
4.875
Axis Length (A)
α-phase
β'-phase
β-phase
0.0
0.5
1.0
1.5
2.0
2.5
3.0
3.5
4.0
4.5
Pressure (GPa)

(a)

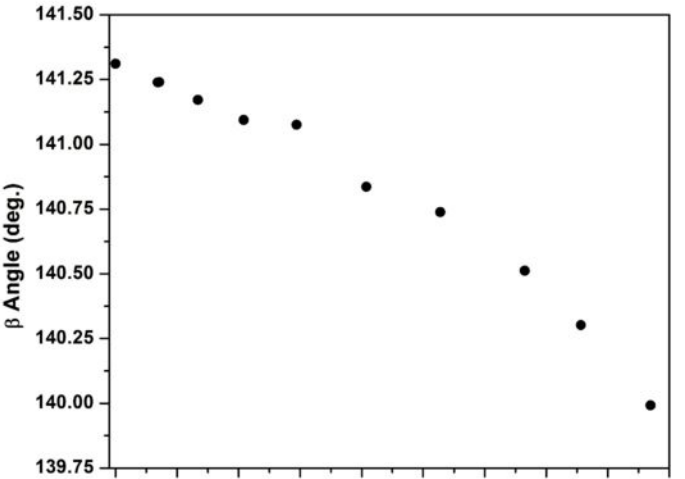
141.50
141.25
141.00
140.75
140.50
140.25
140.00
139.75
β Angle (deg.)
0.0
0.5
1.0
1.5
2.0
2.5
3.0
3.5
4.0
4.5
Pressure (GPa)

(b)

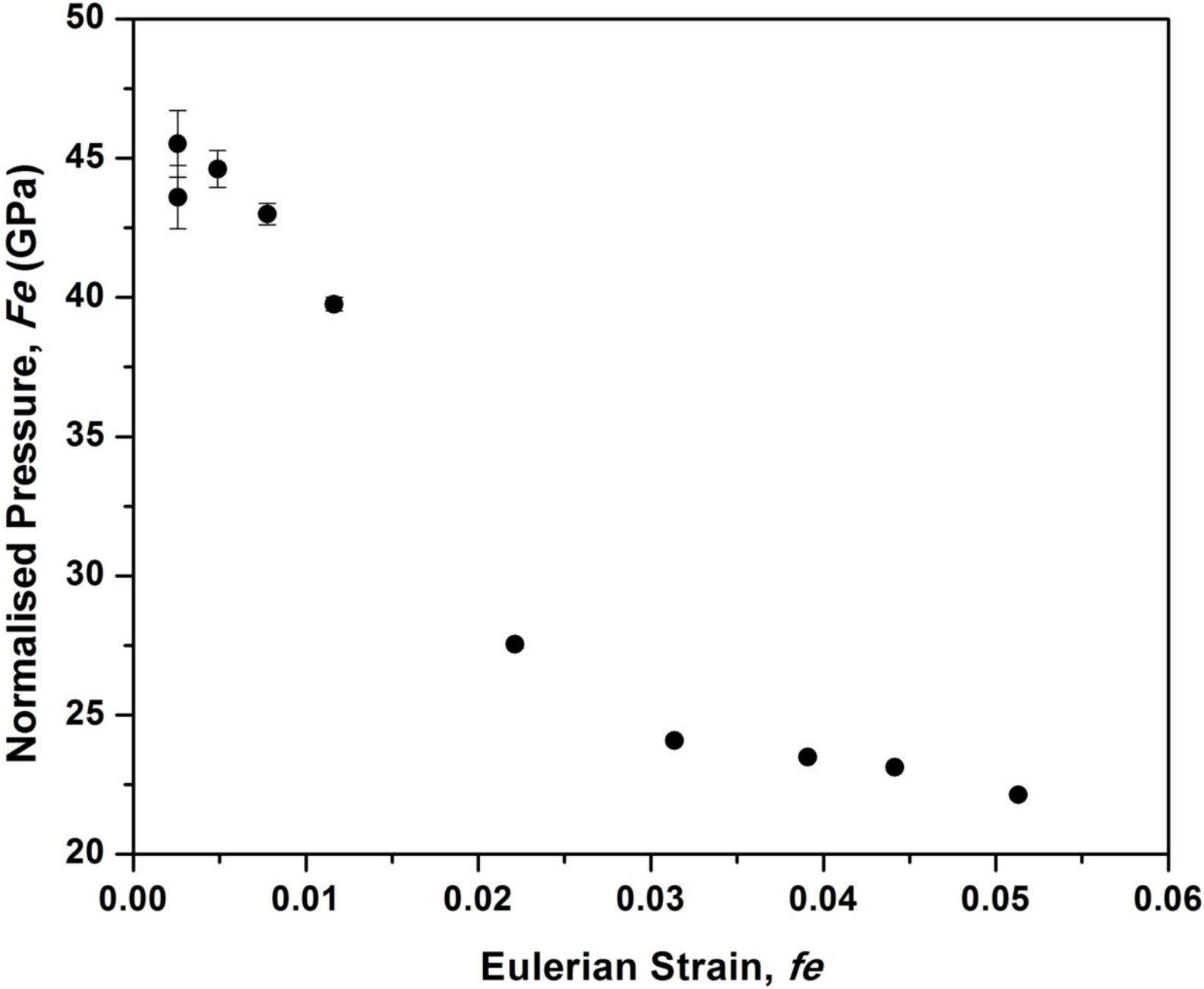
Normalised Pressure, Fe (GPa)
50
45
40
35
30
25
20
0.00
0.01
0.02
0.03
0.04
0.05
0.06
Eulerian Strain, fe

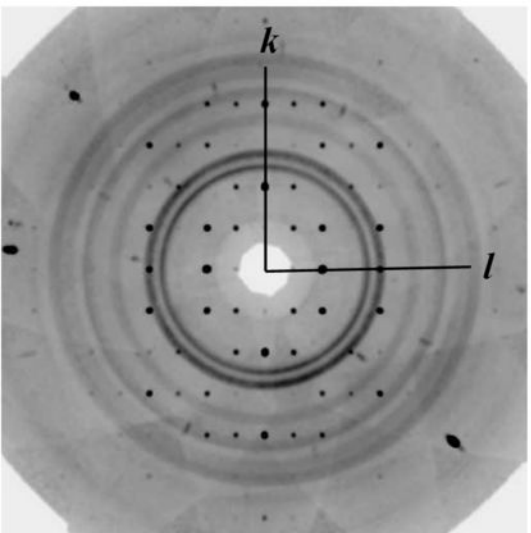
k
l

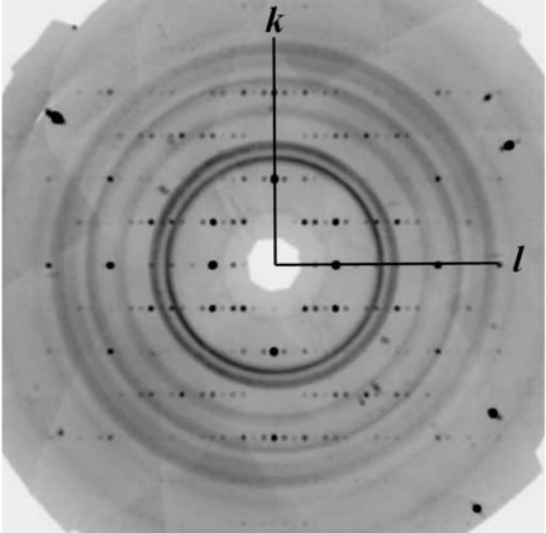
k
l

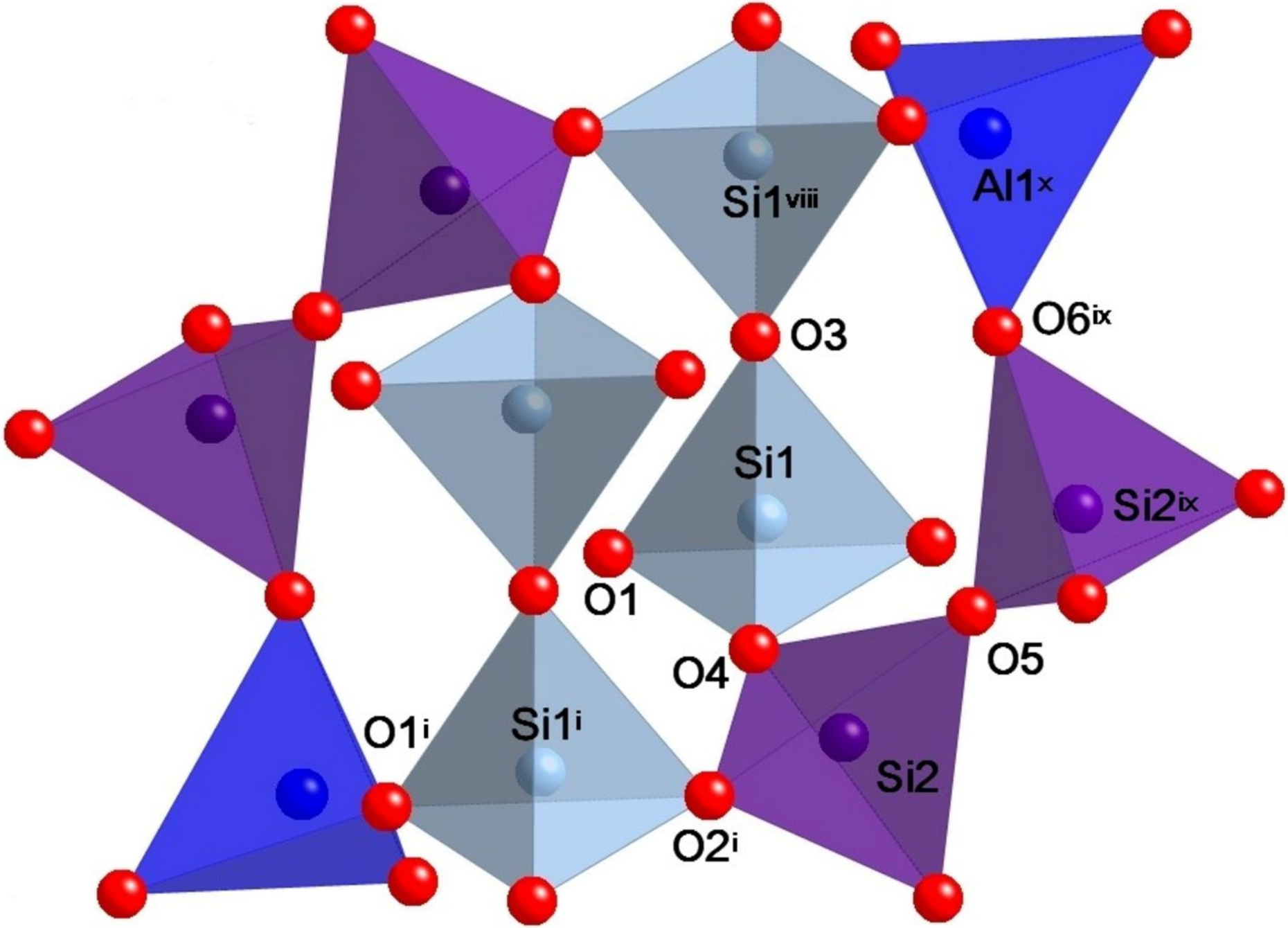
Si1viii
Al1x
O3
O6ix
Si1
Si2ix
O1
O4
O5
O1i
Si1i
Si2
O2i

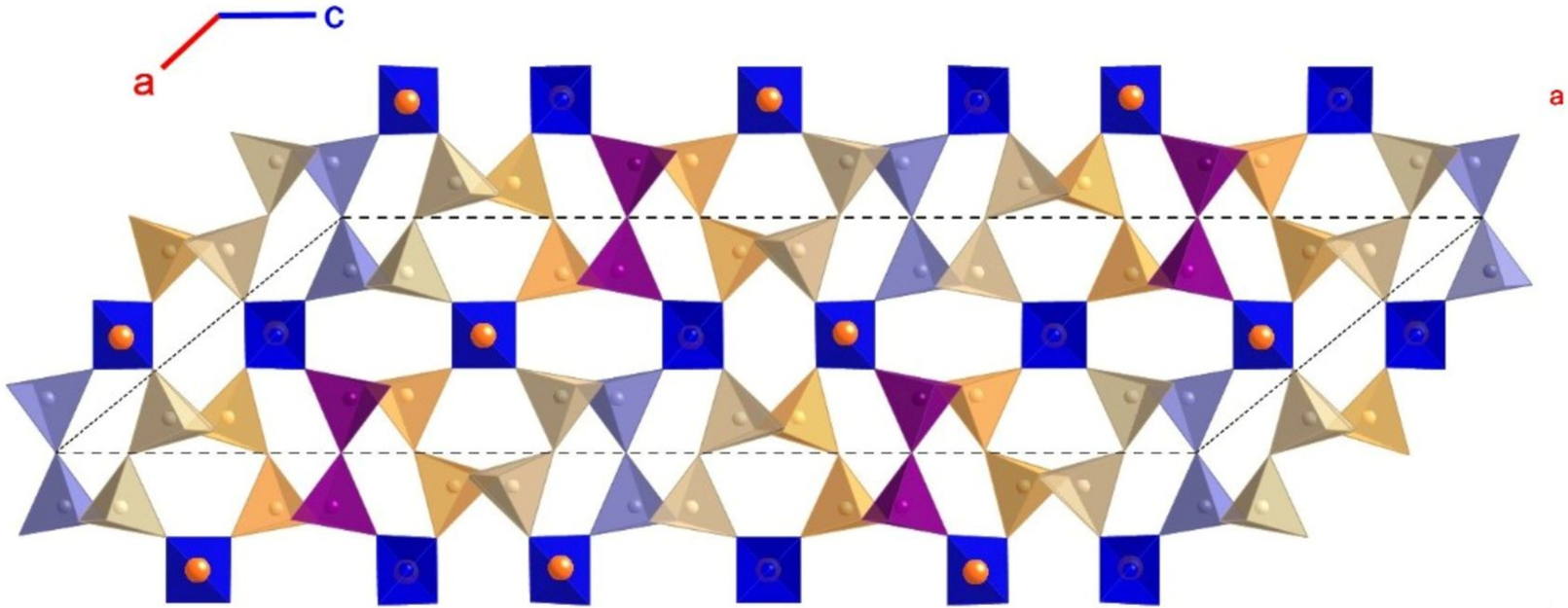

(a)

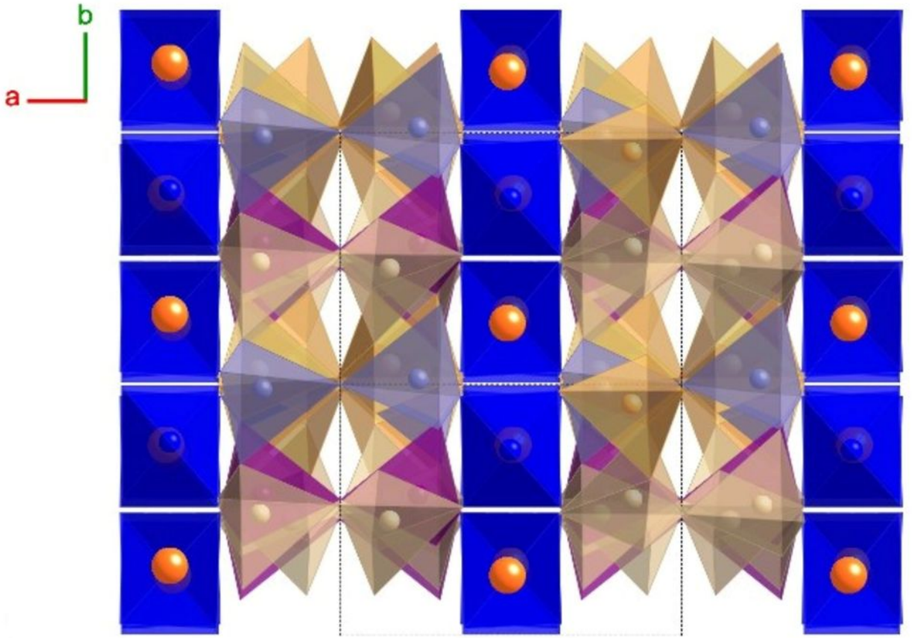

(b)

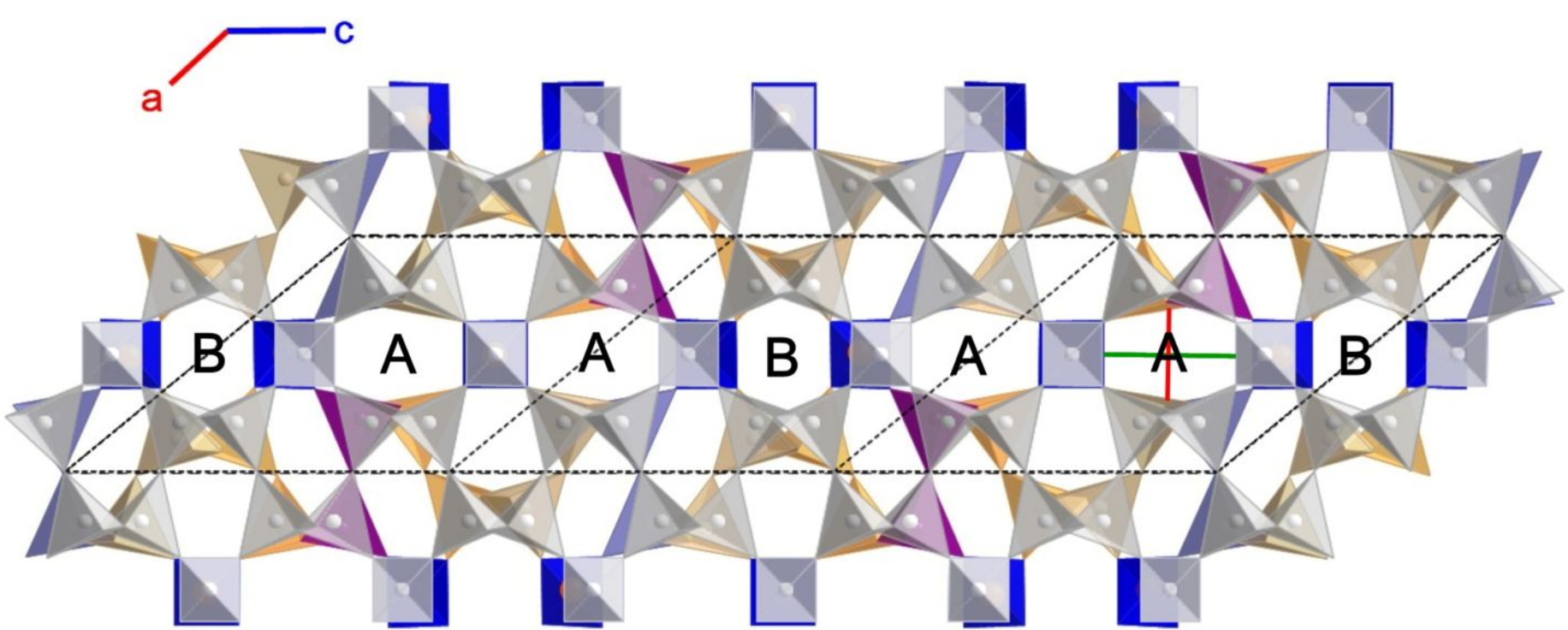
c
a
B
A
A
B
A
A
B